Supplementary Note 1: System layouts and characteristics of LEDs

Supplementary Fig. 1 shows the circuit layouts of peripheral **(Supplementary Fig. 1a**; top) and spinal epidural devices (**Supplementary Fig. 1b**; top), and the respective component information (**Supplementary Fig. 1a-b**; bottom). The harvesting unit is an impedance matching circuit consisting of a ceramic chip capacitor (1 pF; 0.20 mm width, 0.4 mm length, 0.22 mm thickness; bonded by solder paste) and an inductor (2.7 nH; 0.20 mm width, 0.4 mm length, 0.22 mm thickness; bonded by solder paste) connected in series. The rectifier uses miniaturized Schottky diodes (1.7 mm width, 1.5 mm length, 0.5 mm thickness) and ceramic chip capacitors (5 pF; 0.20 mm width, 0.4 mm length, 0.22 mm thickness; bonded by solder paste). The multiplier includes three Schottky diodes identical to those in the rectifier, and boosts voltages provided by the rectifier (~0.9 V) to values sufficient to operate the LEDs (~2.7 V; 220 μm width, 270 μm length, and 50 μm thickness for spinal device; 1.6 mm length, 0.8 mm width, and 0.75 mm thickness for peripheral devices). Electrical characteristics of the LEDs appear in **Supplementary Fig. 2**. The built-in voltage is 2.7 V and the peak emission wavelengths are 470 nm (APT1608LVBC/D, Kingbright) and 465 nm (C460TR2227-0216, Cree Inc.) to match the absorption characteristics of channelrhodopsin (**Supplementary Fig. 2a**). The current-voltage (**Supplementary Fig. 2b**) and optical power density-current (**Supplementary Fig. 2c**) graphs shows a current of 0.6 mA at 2.7 V, and output power density of ~10 mW/mm^2 at 0.6 mA. The LED has a radiation angle of 120 º.

The stress-strain curves of the PDMS layer and the full system were measured with the Q800-Dynamic Mechanical Analysis (DMA) system (TA Instruments) (**Supplementary Fig. 3**). Both samples were prepared with dimensions of 20 mm length, 10 mm width, and 0.5 mm thickness. The elastic Young's modulus is ~ 0.5 MPa for the PDMS alone with stretching up to 100 %, and ~ 1.7 MPa for the full device with stretching up to 40 % before operation failure occurred.

Supplementary Note 2: Center frequencies dependency on hydration

For antennae implanted in biological tissues, one thing that can impact the center frequency of the antenna is hydration status. In order to assess how hydration affects antenna function, we performed simulations. In these calculations, we used the Cole-cole relaxation dielectric model below and parameters for dry and wet skin described in the reference section.[1,2]

$$\varepsilon_r(\omega) = \varepsilon_\infty + \sum_n \frac{\Delta\varepsilon_n}{1 + (iw\tau_n)^{(1-\alpha_n)}} + \frac{\delta_i}{iw\varepsilon_0}$$

where δ is conductivity, τ is the relaxation time constant, ε_0 is the static relative permittivity, and ε_r is the relative permittivity.

The wide bandwidth (200 MHz) of the stretchable antenna allows it to harvest RF power from a much wider range of transmitting frequencies than conventional patch antennae (bandwidth ~50 MHz) (**Supplementary Fig. 4d**). This characteristic reduces the likelihood that a mismatch between the receiver and transmitter will prevent device activation. Based on this model, if the center frequency of an antenna implanted in an animal shifts from 2.33 GHz to 2.25 GHz due to changing physiological conditions or strains, the patch antenna harvests less than 10 % as much power as it did before the shift, while the stretchable antenna still harvests more than 90 % (**Supplementary Fig. 4c)**. This result suggests that the stretchable antenna can function efficiently in biological environments despite changes in the temperature or hydration of the surrounding materials, or the application of strain.

Simulation results reveal that the center frequency shifts toward lower frequencies when implanted under wet skin compared to dry skin (**Supplementary Fig. 5a)**. This shift confirms that the electromagnetic characteristics of biological tissues depend on hydration condition, and that wet tissues are more dispersive than dry tissues. Mechanical simulations show how strain affects center frequencies under both wet and dry tissue (**Supplementary Fig. 5b**). While this simulation suggests that shifts in the center frequency can arise from strain underneath wet tissue, an antenna with a wide bandwidth center frequency can undergo these shifts and remain operational and efficient without changing the transmission wavelength.

Supplementary Note 3: Thermal measurements

We put the implantable devices inside hydrogel that has similar thermal properties to biological tissues. The devices and gel were warmed to 37 ^{o}C using a hot plate to simulate biological temperatures. The harvester was powered wirelessly and operated under the same conditions that

are used in behavior tests (10 mW/mm^2 optical output density, 20 Hz pulse and 10 ms duration for 10 mins). Variations in temperature due to device activation were monitored with ultrathin thermal sensors which were implanted at three different positions between the LED and the hydrogel (**Supplementary Fig. 9a)**. Modeling data were used to compare the results for each temperature probe (**Supplementary Fig. 9b).** The results show transient heating at the LED surface that is correlated with pulsed operation of the LED (20 Hz, 10 ms duration). Transient but minute heating is also detected at the PDMS tube-hydrogel interface 190 μm away from the LED (**Supplementary Fig. 9c-e**). There were no noticeable variations (< 0.1 ^{o}C) of temperature when the sensor was 440 μm from the LED (**Supplementary Fig. 9c-e**).

Supplementary Note 4: TX efficiency for activation of peripheral nerve devices

Incident RF radiation and its coupling into a dynamically moving antenna are crucial to the utility of these devices. The efficiency of RF coupling can be described using the transmission coefficient (S_{12}), the optical power density, and the angular radiation patterns. All three of these parameters, which are calculated here using simulations, are necessary to fully describe the characteristics of RF harvesting with wireless devices.

S_{12} corresponds to the logarithm of the fraction of an electromagnetic wave that passes through a surface. A large S_{12} indicates efficient coupling between the TX and receiving systems (**Supplementary Fig. 11a**), but the S_{12} can vary with antenna positioning. In the case of devices implanted in freely-behaving animals, S_{12} varies with different activities such as walking, standing, or lying down. To assess the effect of this variation on device operation, the values of S_{12} for walking, standing, and lying were calculated and normalized to the value of S_{12} for walking. The S_{12} at a frequency of 2.34 GHz for walking, standing, and lying are 0, -0.42, and -0.93 (**Supplementary Fig. 11a**). This means that if the antenna receives 100 μW while the mouse is walking it would receive 89.5 μW and 98.2 μW if the mouse were instead standing on its hind legs or lying down. A reduction of received power by 10-20 % corresponds to a reduction of 3-6 % in simulated optical output power due to the conversion efficiency of the LEDs (30 %).

Calculations for S_{12} indicate the total optical power density available as a function of position across the cage. These levels lie within an acceptable range for optogenetic activation (**Supplementary Fig. 11b-d;** right**)**. To supplement the simulations, measurements of optical power density along the bottom of a cage (**Supplementary Fig. 10a**) and maps of simulated optical power density as a function of the distance from the bottom of the cage were generated (**Supplementary Fig. 10b-g**). The results are consistent with the modeling data (**Supplementary Fig. 10h-l**). The power delivered to the device depends also on the orientation, as determined by the angular radiation patterns, which allow the calculation of the area of overlap between the TX antenna and the implantable antenna; increases in the overlap of radiation patterns associated with the TX antenna and the receiving antenna correspond to improved coupling.[3] Walking and standing postures involve orientations that both yield ~33 % areas of overlap, due to similar radiation and coupling patterns (**Supplementary Fig. 11b-d;** middle). Somewhat reduced coupling (~27 % area of overlap) occurs in the lying posture due to loss of power associated with transmission through biological tissues (**Supplementary Fig. 11d;** middle). The results suggest that wireless activation of the sciatic nerve devices will be consistent and uniform for all mouse orientations and locations.

Supplementary Note 5: TX configuration for activation of spinal cord regions

The efficiency of RF coupling must also be assessed for the epidural devices (**Supplementary Fig. 12a**), in addition to the peripheral nerve devices described in **Supplementary Note 4**. S_{12} for the antenna used in the epidural devices at 2.24 GHz when the mice are walking, standing, or lying down is -0.68, -0.1, and 0 (**Supplementary Fig. 12b**). This result shows that if the antenna receives 91.6 μW while walking, it would receive of 99.2 μW and 100 μW if the mouse were instead standing on its hind legs or lying down. A reduction in the received power by 10-20 % corresponds to a reduction of 3-6 % in optical output power due to the conversion efficiency of LEDs (30 %). The conclusions based on S_{12} are reinforced by the angular radiation patterns of the antenna (**Supplementary Fig. 12c-e;** left). In these plots, increases in the overlap of radiation patterns associated with the TX antenna and the receiving antenna correspond to improved coupling. The lying and standing postures both yield ~33 % areas of overlap, because these cases involve orthogonal orientation to the TX antennas, with similar radiation and coupling patterns (**Supplementary Fig. 12d-e;** left). Somewhat reduced coupling (~29 % area of overlap) occurs

when walking due to loss of power associated with transmission through biological tissues (**Supplementary Fig. 12c;** left).[4, 5] Collectively, the S_{12} and angular radiation patterns show that this transmission configuration allows uniform wireless activation of epidural devices within the targeted area regardless of mouse orientation or location (**Supplementary Fig. 12c-e;** right).

Supplementary Note 6: Generating the mouse lines for optogenetic studies

A transgenic cre-recombinase approach was used to generate mice with ChR2 expression limited to nociceptors by crossing heterozygous TrpV1-Cre mice with homozygous Ai32 mice, producing a TrpV1-ChR2 line (**Supplementary Fig. 13a**), or by crossing heterozygous SNS-Cre mice to Ai32 mice, producing a SNS-ChR2 line (**Supplementary Fig. 14a**). Details of these lines and crosses are provided in **Online Methods**.

Supplementary Note 7: Electrophysiological characterization of ChR2 expressing dorsal root ganglia neurons

Whole-cell patch clamp recordings from cultured dorsal root ganglia (DRG) neurons from adult Advillin-ChR2 mice demonstrate large inward photocurrents in response to blue light illumination (470 nm, 10 mW/mm^2), confirming functional channel expression and trafficking in peripheral neurons (**Figure 3b,** bottom trace). Current-clamp recordings reveal persistent action potential firing in response to constant illumination in some neurons (**Figure 3b,** top trace), while in others only a single action potential is elicited at the onset of illumination. Similarly, we are able to drive firing with high fidelity using short pulses of light at defined frequencies up to 20 Hz in some cells (**Figure 3c**), but many cells fire at lower fidelity. Detailed electrophysiological characteristics of TrpV1-ChR2 dorsal root ganglion neurons can be found in **Supplementary Table 2**. These data and previous studies[6] demonstrate that neuronal output in ChR2-expressing sensory neurons can be controlled using blue light. Similar data demonstrating the excitability of TrpV1-ChR2 or SNS-ChR2 neurons with light are included in **Supplementary Fig. 13b-c and 14b-c.**

Supplementary Note 8: Immunohistological characterization of ChR2 expression

Immunohistochemical analysis of adult Advillin-ChR2 mice confirms ChR2 expression along all axes of the peripheral nervous system. Centrally projecting axons expressing ChR2 are found

throughout the spinal cord dorsal horn (green, **Figure 3d**), including nociceptive fibers that terminate in lamina I and II where they are co-labeled with IB4 (non-peptidergic nociceptors, red) or CGRP (peptidergic nociceptors, purple). Staining of the dorsal root ganglion reveals ChR2 expression in most neurons, as confirmed by co-expression with the neuron-specific microtubule protein βIII-tubulin (green and purple, **Figure 3e**). Additionally, all neurons that bind IB4 (red) express ChR2 (green, **Figure 3e**). We also confirmed that ChR2 was efficiently trafficked in peripherally-projecting axons. Longitudinal- (**Figure 3f**) and cross-sections (**Figure 3g**) of the sciatic nerve show robust ChR2 expression along the fibers, which is observed in a subset of myelinated axons marked by NF200 (purple).

Immunohistochemical analysis of adult Advillin-ChR2 mice confirms ChR2 expression in the dorsal root ganglion. There is significant overlap of ChR2-EYFP (green) expression with βIII tubulin (purple) within the soma (**Supplementary Fig. 15a** 82 ± 3 %). There is also significant expression of ChR2-EYFP (green) within the subpopulation of non-peptidergic neurons, identified through labeling for IB4 (red) (**Supplementary Fig. 15b-c** 29 ± 6 %) and the subpopulation of peptidergic neurons, identified through labeling for CGRP (blue) (**Supplementary Fig. 15b-c** 57 ± 8 %).

Immunohistochemical analysis of adult TrpV1-ChR2 mice confirms ChR2 expression along all axes of the peripheral nervous system. Centrally projecting axons expressing ChR2 are found throughout the spinal cord dorsal horn (green, **Supplementary Fig. 13d**), including nociceptive fibers that terminate in lamina I and II where they are co-labeled with IB4 (non-peptidergic nociceptors, red) or CGRP (peptidergic nociceptors, purple). Staining of the dorsal root ganglion reveals ChR2 expression in many neurons, as confirmed by co-expression with the neuron-specific microtubule protein βIII-tubulin (green and purple, **Supplementary Fig. 13e**). We also confirmed that ChR2 was efficiently trafficked in peripherally-projecting axons. Longitudinal- (**Supplementary Fig. 13f**) and cross-sections (**Supplementary Fig. 13g**) of the sciatic nerve show robust ChR2 expression along the fibers, which is observed in a subset of myelinated axons marked by NF200 (purple).

Immunohistochemical analysis of adult TrpV1-ChR2 mice confirms ChR2 expression in the

dorsal root ganglion. There is significant overlap of ChR2-EYFP (green) expression with βIII tubulin (purple) within the soma (**Supplementary Fig. 16a** 59 ± 3 %). There is also significant expression of ChR2-EYFP (green) within the subpopulation of non-peptidergic neurons, identified through labeling for IB4 (red) (**Supplementary Fig. 16b-c** 41 ± 5 %) and the subpopulation of peptidergic neurons, identified through labeling for CGRP (blue) (**Supplementary Fig. 16b-c** 51 ± 7 %).

Immunohistochemical analysis of adult SNS-ChR2 mice confirms ChR2 expression along all axes of the peripheral nervous system. Centrally projecting axons expressing ChR2 are found throughout the spinal cord dorsal horn (green, **Supplementary Fig. 14d**), including nociceptive fibers that terminate in lamina I and II where they are co-labeled with IB4 (non-peptidergic nociceptors, red) or CGRP (peptidergic nociceptors, purple). Staining of the dorsal root ganglion reveals ChR2 expression in many neurons, as confirmed by co-expression with the neuron-specific microtubule protein βIII-tubulin (green and purple, **Supplementary Fig. 14e**). We also confirmed that ChR2 was efficiently trafficked in peripherally-projecting axons. Longitudinal- (**Supplementary Fig. 14f**) and cross-sections (**Supplementary Fig. 14g**) of the sciatic nerve show robust ChR2 expression along the fibers, which is observed in a subset of myelinated axons marked by NF200 (purple).

Immunohistochemical analysis of DRG neurons of adult SNS-ChR2 mice has been previously described in the literature. We also confirmed that ChR2 expression is absent in ventral horn motor neurons in all three mouse lines (**Supplementary Fig. 17**).

Reference

1. Park, S.-I. Enhancement of Wireless Power Transmission into Biological Tissues Using a High Surface Impedance Ground Plane. *PIER* **135**, 123-136 (2013).
2 Gabriel, S. The dielectric properties of biological tissues:III.Parametric models for the dielectric spectrum of tissues. Phy. in Med. and Bio. **41**,2271-2293 (1996).
3. Harrington, R.F. Time-Harmonic Electromagnetic Fields 2nd edn *Wiley-IEEE Press*. (2001).
4. Engineers, I.f.E.a.E., Vol. C95.1-2005 (2005).
5. Park, S.-I. et al. Ultraminiaturized photovoltaic and radio frequency powered optoelectronic systems for wireless optogenetics. *J.Neural Eng.* **12**, 056002 (2015).
6. Daou, I. et al. Remote optogenetic activation and sensitization ofpain pathways in freely moving mice. *J. Neurosci* **33**, 18631-18640 (2013).

a

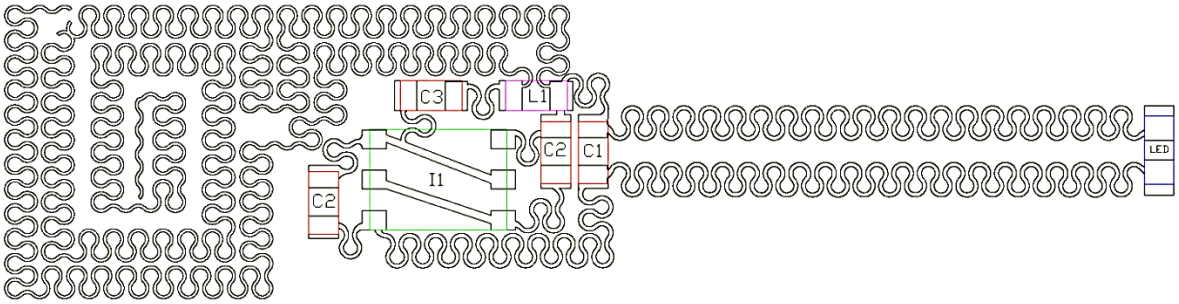

	Components	Product number	Vendor information
LED	470 nm, 1.6 mm x 0.8 mm x 0.7 mm	APT1608LVBC/D	Kingbright
C1,3	Capacitor, 1 pF, 0.2 mm x 0.4 mm x 0.22 mm	250R05L1R0BV4T	Johanson Technology
C2	Capacitor, 5 pF, 0.6 mm x 0.3 mm x 0.33 mm	250R05L5R1CV4T	Johanson Technology
I1	Schottky diode, 1.7 mm x 1.5 mm x 0.5 mm	1PS66SB82,115	NXP Semiconductor
L1	Inductor, 2.7 nH, 0.2 mm x 0.4 mm x 0.22 mm	L-05B2N7SV6T	Johanson Technology

b

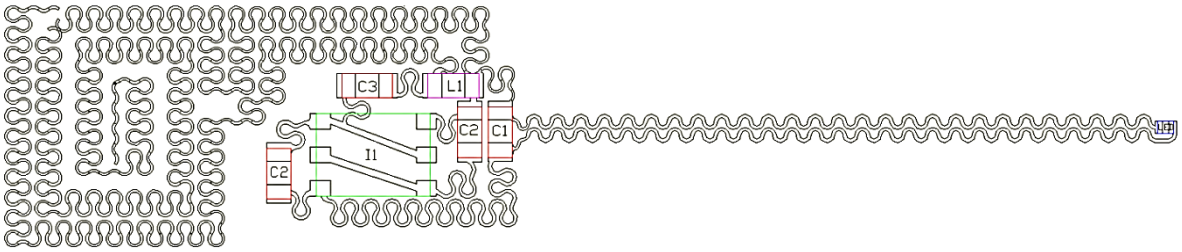

	Components	Product number	Vendor information
LED	465 nm, 0.22 mm x 0.27 mm x 0.05 mm	C460TR2227-0216	Cree Inc.
C1,3	Capacitor, 1 pF, 0.2 mm x 0.4 mm x 0.22 mm	250R05L1R0BV4T	Johanson Technology
C2	Capacitor, 5 pF, 0.6 mm x 0.3 mm x 0.33 mm	250R05L5R1CV4T	Johanson Technology
I1	Schottky diode, 1.7 mm x 1.5 mm x 0.5 mm	1PS66SB82,115	NXP Semiconductor
L1	Inductor, 2.7 nH, 0.2 mm x 0.4 mm x 0.22 mm	L-05B2N7SV6T	Johanson Technology

Supplementary Fig. 1 Component information for the sciatic and epidural LED devices. Layout and component information of (a) Sciatic and (b) spinal epidural devices.

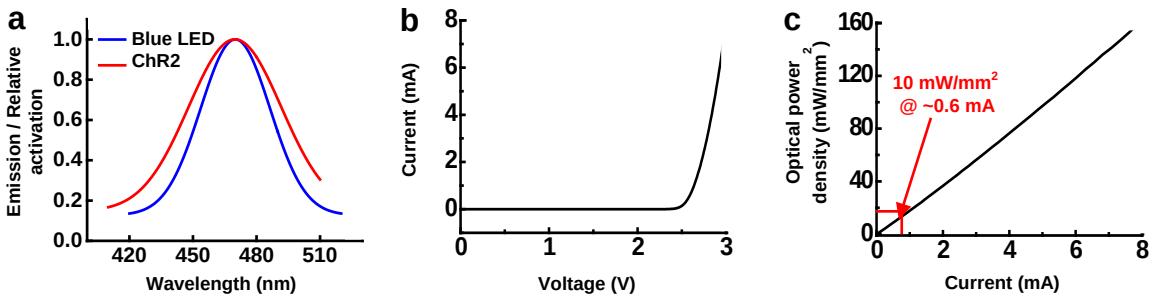

Supplementary Fig. 2

Overview of system characteristics. (a) Comparison of the emission spectrum of blue LEDs used in the devices and the absorption spectrum of Channelrhodopsin (ChR2). (b) Current-Voltage (I-V) characteristics of LEDs. (c) Light output power of the LEDs as a function of electrical input current.

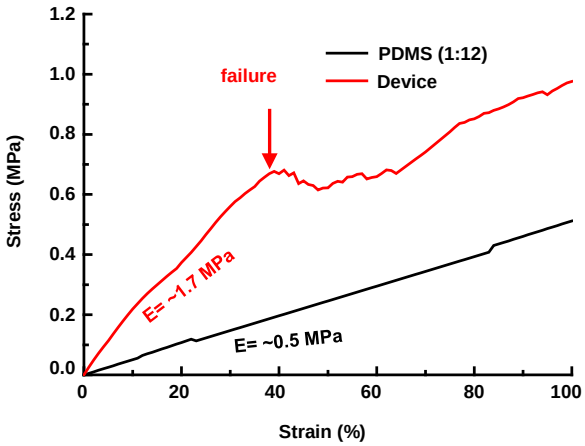

Supplementary Fig. 3

Mechanical stress limits of wireless LED devices. Stress-strain curves of the PDMS layer alone (black) and the complete implantable devices (red) under up to 100 % stretching using a Q800-DMA. The PDMS alone has a Young's modulus of 0.5 MPa with stretching of up to 100 %, while the implantable device has a Young's modulus of ~ 1.7 MPa with stretching of up to 40 % before operation failure occurs.

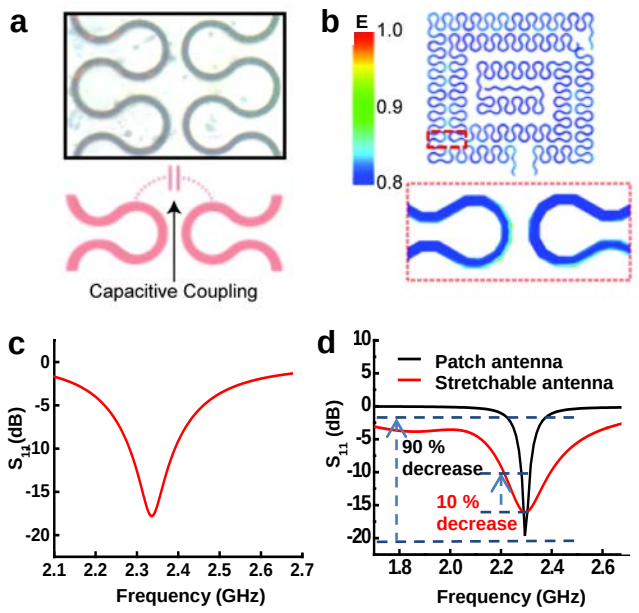

Supplementary Fig. 4

Capacitive coupling performance of stretchable antennae. (a) Exploded view of a stretchable antenna (top), schematic view of constituent serpentine wires (bottom). (b) Normalized electric field distributions on a stretchable antenna (top) and exploded view (bottom). (c) Scattering parameter, S_{11}, of a stretchable antenna in its undeformed configuration as a function of transmission frequency. (d) Comparison of the S_{11} of a stretchable antenna (red) and patch antenna (black). The bandwidth of the center frequency of the stretchable antenna (200 MHz) is significantly wider than that of the patch antenna (~50 MHz).

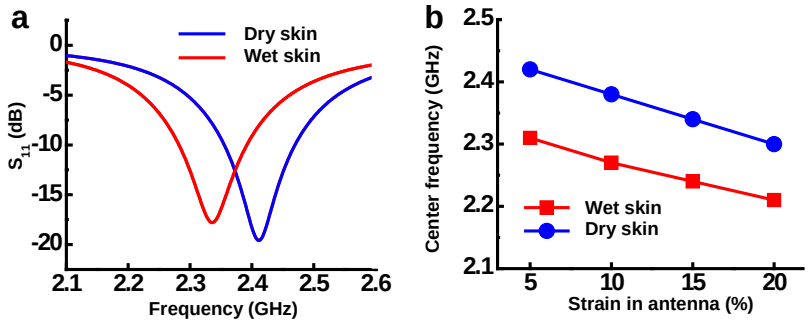

Supplementary Fig. 5

Characteristics of the stretchable antenna under wet and dry skin. (a) The scattering parameter, S_{11}, of the stretchable antenna under wet skin (red) and dry skin (blue). (b) Deviations of the center frequencies as a function of strain under wet skin (red) and dry skin (blue).

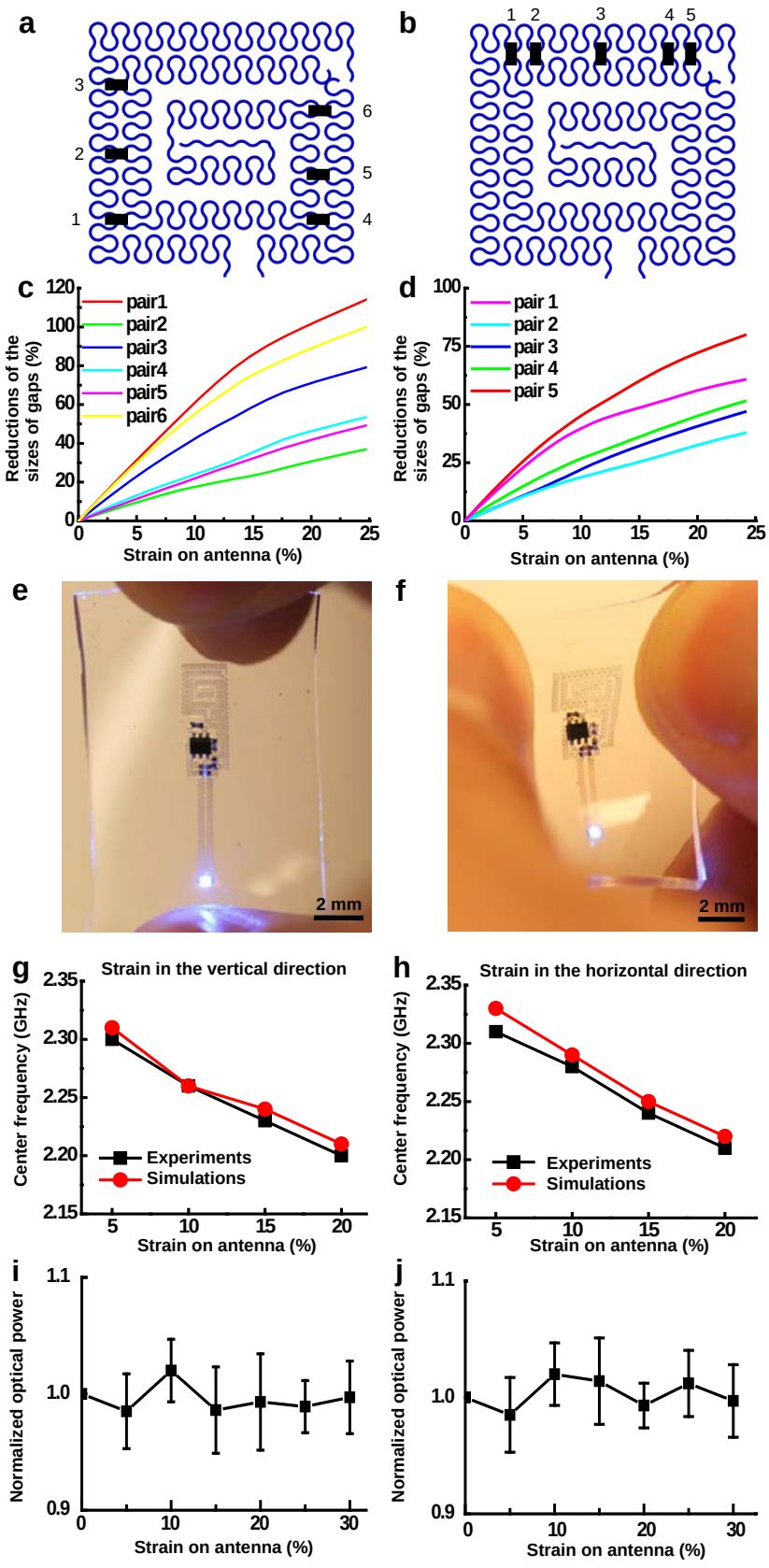
a
1
2
3
4
5
6
b
1 2 3 4 5
c
Reductions of the sizes of gaps (%)
Strain on antenna (%)
pair1
pair2
pair3
pair4
pair5
pair6
d
Reductions of the sizes of gaps (%)
Strain on antenna (%)
pair 1
pair 2
pair 3
pair 4
pair 5
e
2 mm
f
2 mm
g
Strain in the vertical direction
Center frequency (GHz)
Strain on antenna (%)
Experiments
Simulations
h
Strain in the horizontal direction
Center frequency (GHz)
Strain on antenna (%)
Experiments
Simulations
i
Normalized optical power
Strain on antenna (%)
j
Normalized optical power
Strain on antenna (%)

Supplementary Fig. 6

Mechanical characteristics of the stretchable antenna under strain. Mechanical characteristics of the stretchable antenna when strain is applied in the vertical direction (a), (c), (e), and (g), and in the horizontal direction (b), (d), (f), and (h). (a) Six, (b) five pairs of serpentine lines (modeled pairs are labeled with black bars) were selected to model the effects of the vertical or horizontal strain, respectively. (c), (d) Plots of gap variations versus strain on the antenna. (e), (f) Images of the stretched devices. (g), (h) Plots of center frequency versus strain on antenna based on both experiments (black) and simulations (red). (i), (j) Plots of normalized optical output power versus strain on the antenna.

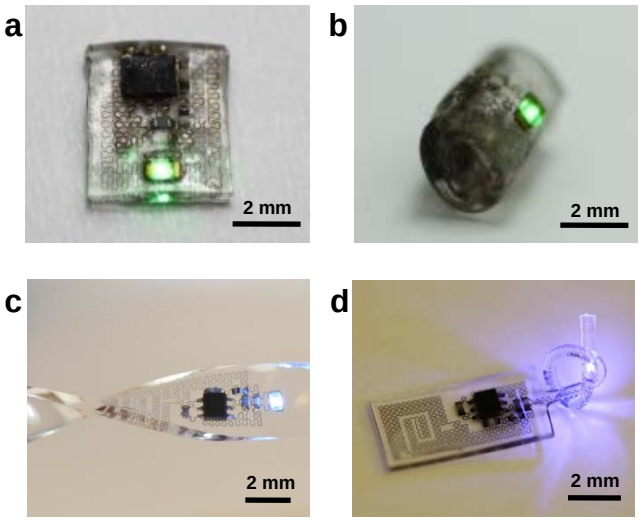

Supplementary Fig. 7

Performance of wireless LED devices under significant physical strain. Demonstrations of wireless operation when a harvester is completely folded in half (a), rolled up with a curvature of 500 μm (b), twisted (c), and knotted with a diameter of 380 μm (d).

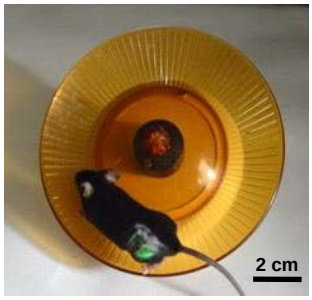

Supplementary Fig. 8

Image of a mouse with a green LED during exercise on a running wheel.

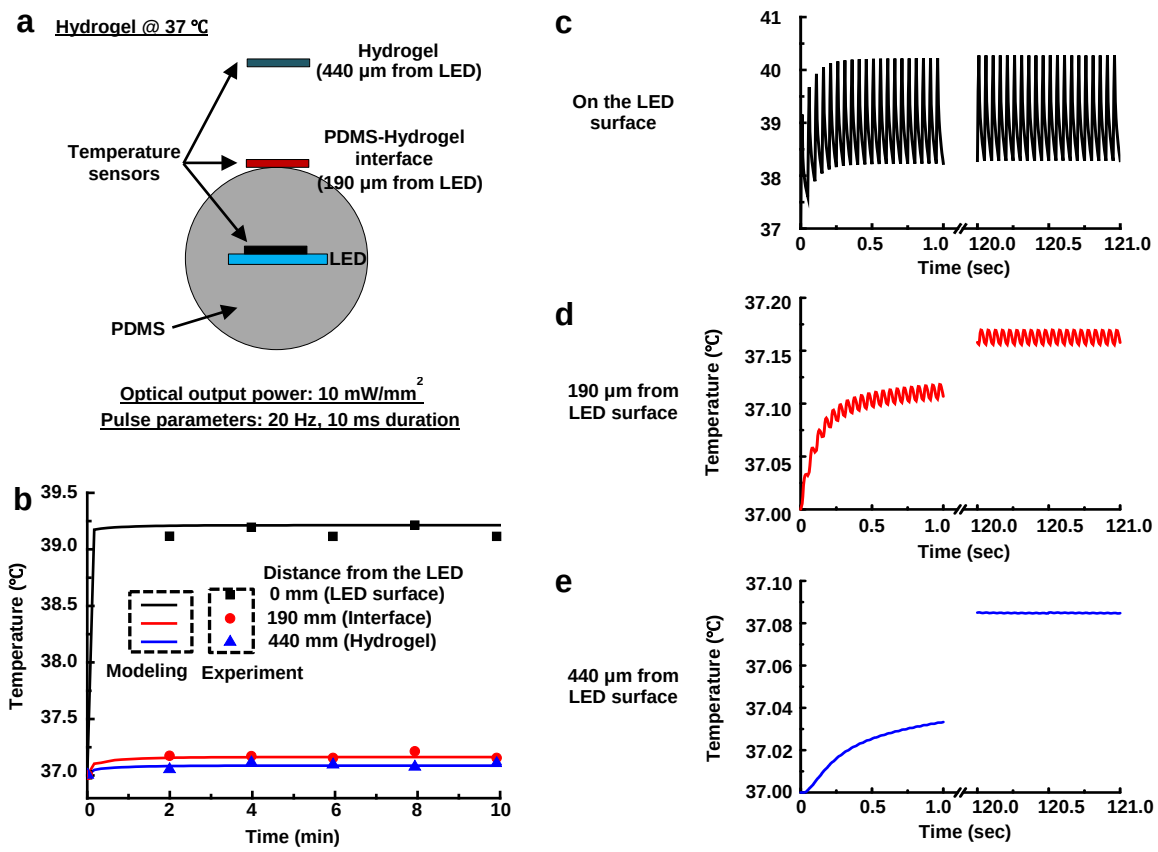

Supplementary Fig. 9

Thermal characteristics of the fully implantable LED devices. Variations of temperature were monitored at various distances (0 μm, 190 μm, or 440 μm) from the heating source (the LEDs). (a) Schematic illustration of temperature measurement, (b) Experimental and modeling results based on the distance from the LED, (c) Temperature on the surface of the LEDs from 1 to 121 seconds after activation (d) Temperature 190 μm away from the LEDs from 1 to 121 seconds after activation (e) Temperature 440 μm away from the LEDs from 1 to 121 seconds after activation.

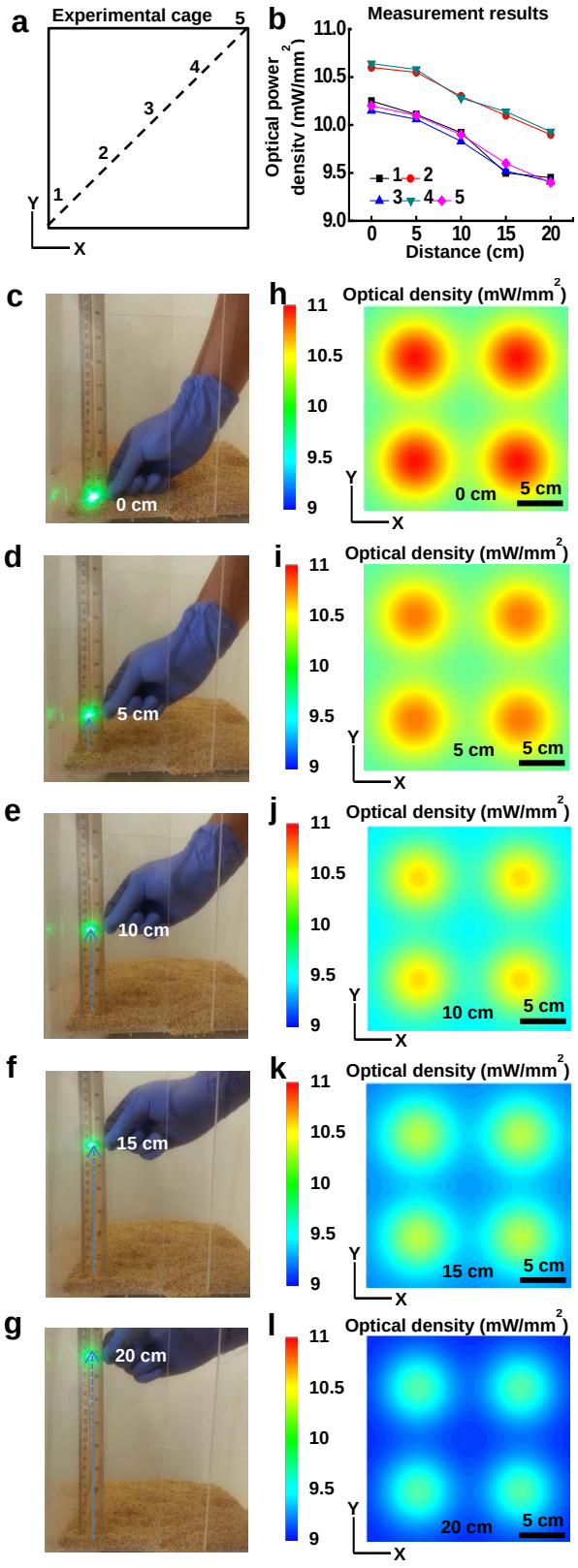
a
Experimental cage
1
2
3
4
5
Y
X
b
Measurement results
Optical power density (mW/mm2)
11.0
10.5
10.0
9.5
9.0
0
5
10
15
20
Distance (cm)
1
2
3
4
5
c
0 cm
d
5 cm
e
10 cm
f
15 cm
g
20 cm
h
Optical density (mW/mm2)
11
10.5
10
9.5
9
0 cm
5 cm
i
5 cm
5 cm
j
10 cm
5 cm
k
15 cm
5 cm
l
20 cm
5 cm

Supplementary Fig. 10

Wireless activation range for devices. (a) Illustration of locations along the cage base where the optical power density was measured. (b) Plot of measured optical power density along the black dotted line at regions 1, 2, 3, 4, and 5. (c)-(g). Images of wireless device operation in a cage at distances of 0, 5, 10, 15, and 20 cm from the antenna underneath the bottom of the cage. (h)-(l) Maps of simulated optical power densities at a distance of 0, 5, 10, 15, and 20 cm from the bottom of the cage.

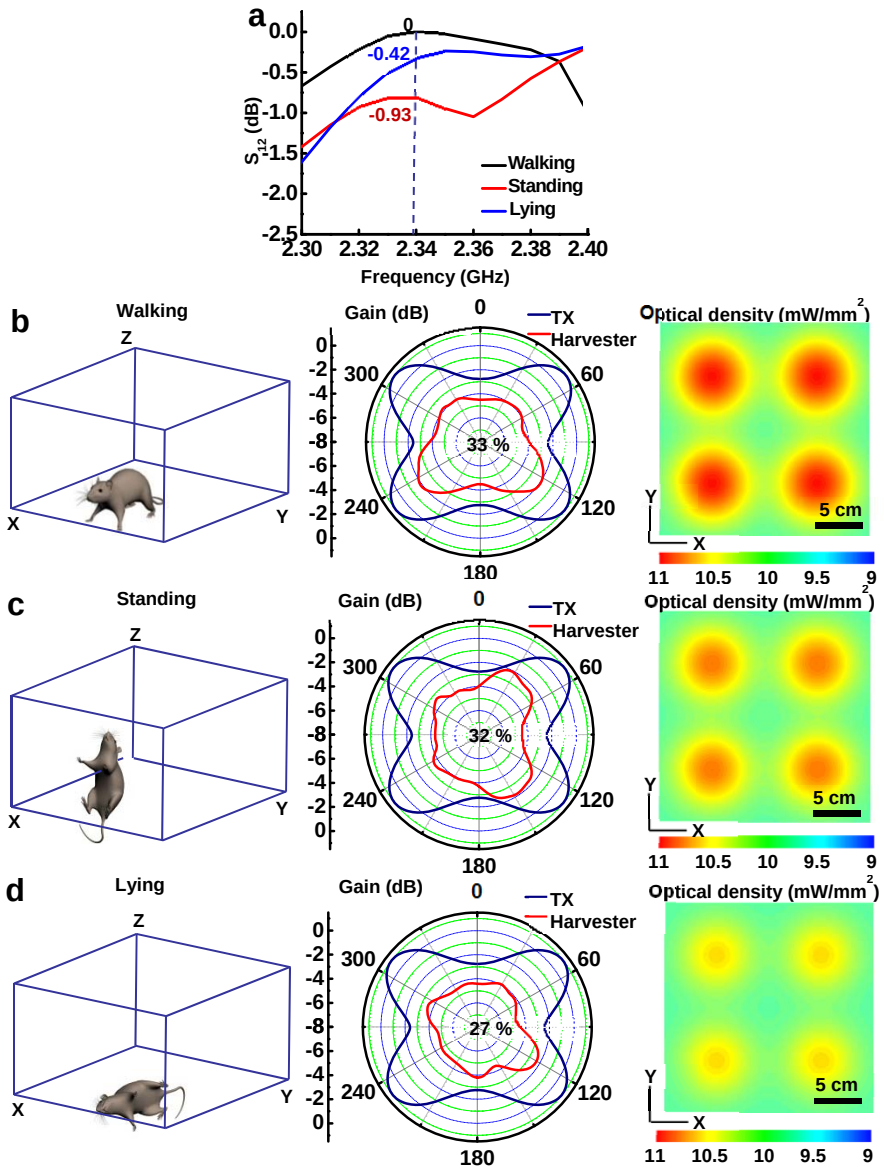

Supplementary Fig. 11

Overview of RF control strategies for peripheral nerve stimulation. (a) S_{12} as a function of frequency when a mouse walks, stands on its hind legs, and lies on its side. (b), (c), and (d) Illustrations of mouse orientation (left), corresponding angular radiation beam patterns (middle: TX system - blue, implanted harvester antennas - red), and associated simulated optical power density (right) when a mouse walks, stands on its hind legs, and lies on its side. The percentile values in the center of the plots of the angular radiation patterns indicate the extent of overlap of radiation patterns of the TX antenna and the harvester antenna.

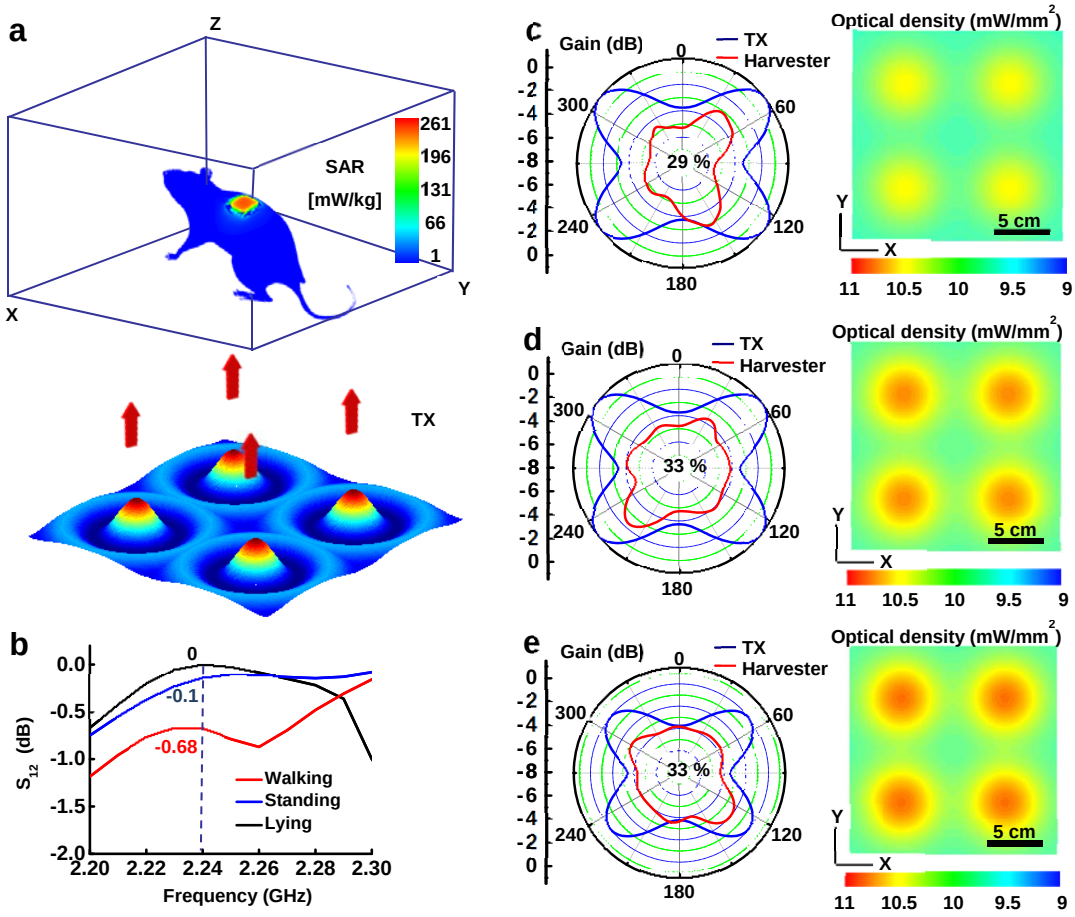

Supplementary Fig. 12

Overview of RF control strategies for spinal cord stimulation. (a) Schematic view of the TX system and an experimental assay with SAR distributions on a mouse mesh body. Multiple antennas are located on the XY plane and placed below the assay. (b) Transmission characteristics, S_{12}, of the TX system at 2.24 GHz when the mouse walks, stands on its hind legs, and lies on its side. (c), (d) and (e) Angular radiation patterns (left: TX system - blue, implanted harvester - red), and associated simulated optical power density (right) when the mouse walks, stands on its hind legs, or lies on its side. The percentile values in the center of the plots of the angular radiation patterns indicate the extent of overlap of radiation patterns of the TX antenna and the harvester antenna.

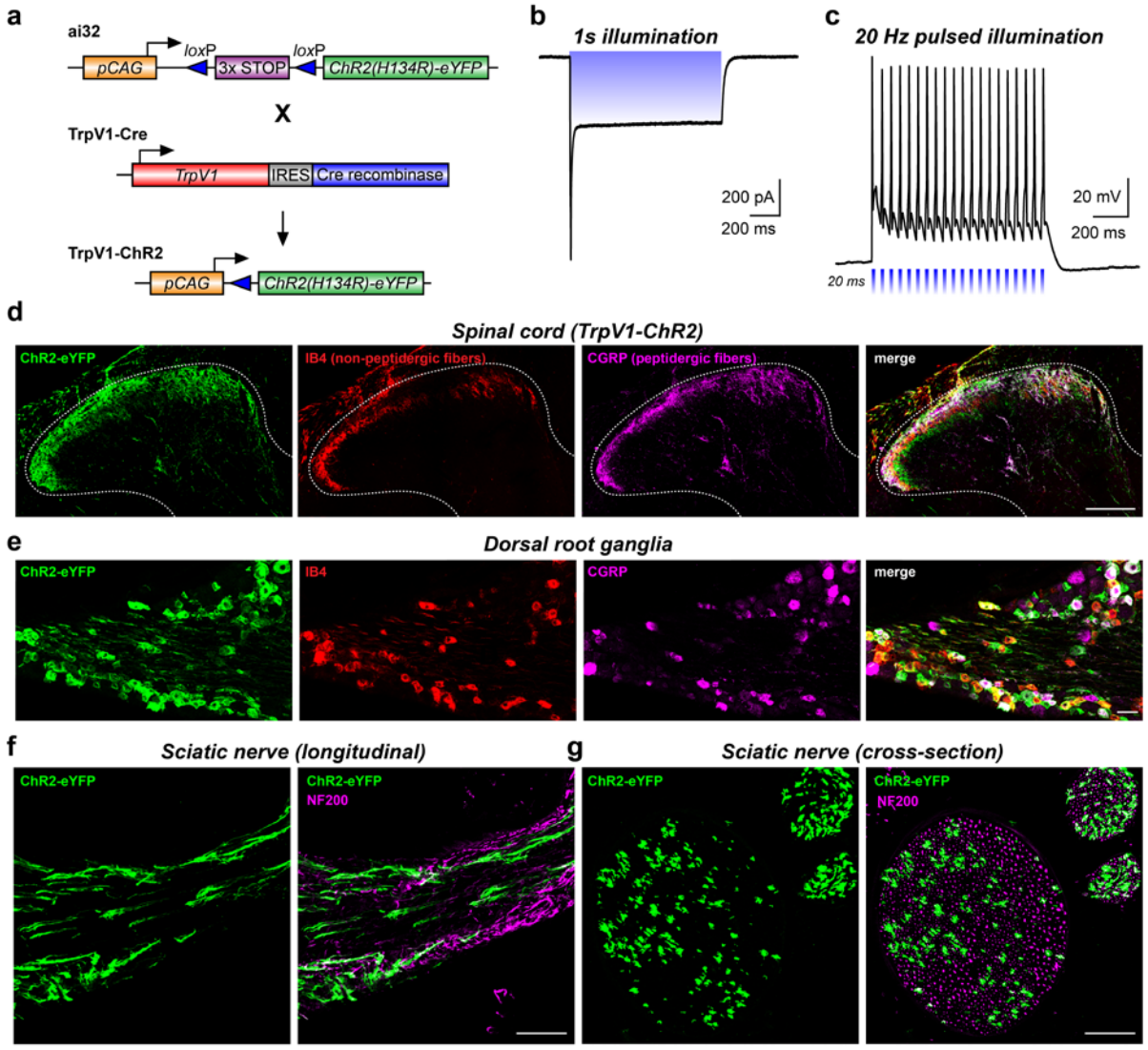

Supplementary Fig. 13

Electrophysiological and anatomical characterization of ChR2 expression in TrpV1-Ai32 mice. (a) Schematic of the Ai32 locus and TrpV1-Cre locus, together with results of the cre-dependent recombination of the Ai32 locus. (b) Inward current in cultured sensory neuron from the TrpV1-ChR2 mice. (c) In current clamp, 20 Hz pulsed illumination results in high-fidelity action potential firing in TrpV1-ChR2 mice. (d) Immunohistochemical analysis of tissue from adult TrpV1-Ai32 mice demonstrates that ChR2 is expressed along the peripheral neuraxis, including termination in lamina I and lamina II of the spinal cord dorsal horn as evidenced by overlap with CGRP (purple) and IB4 (red), respectively. (e) Staining of DRG demonstrates significant overlap of expression with CGRP (purple) and IB4 (red) within the soma, and longitudinal (f) and cross

sections (g) of sciatic nerve demonstrate robust staining along the plasma membrane of the axons. This expression pattern, as expected is more restricted than in Advillin-Ai32 mice. Scale bars = 100 μm.

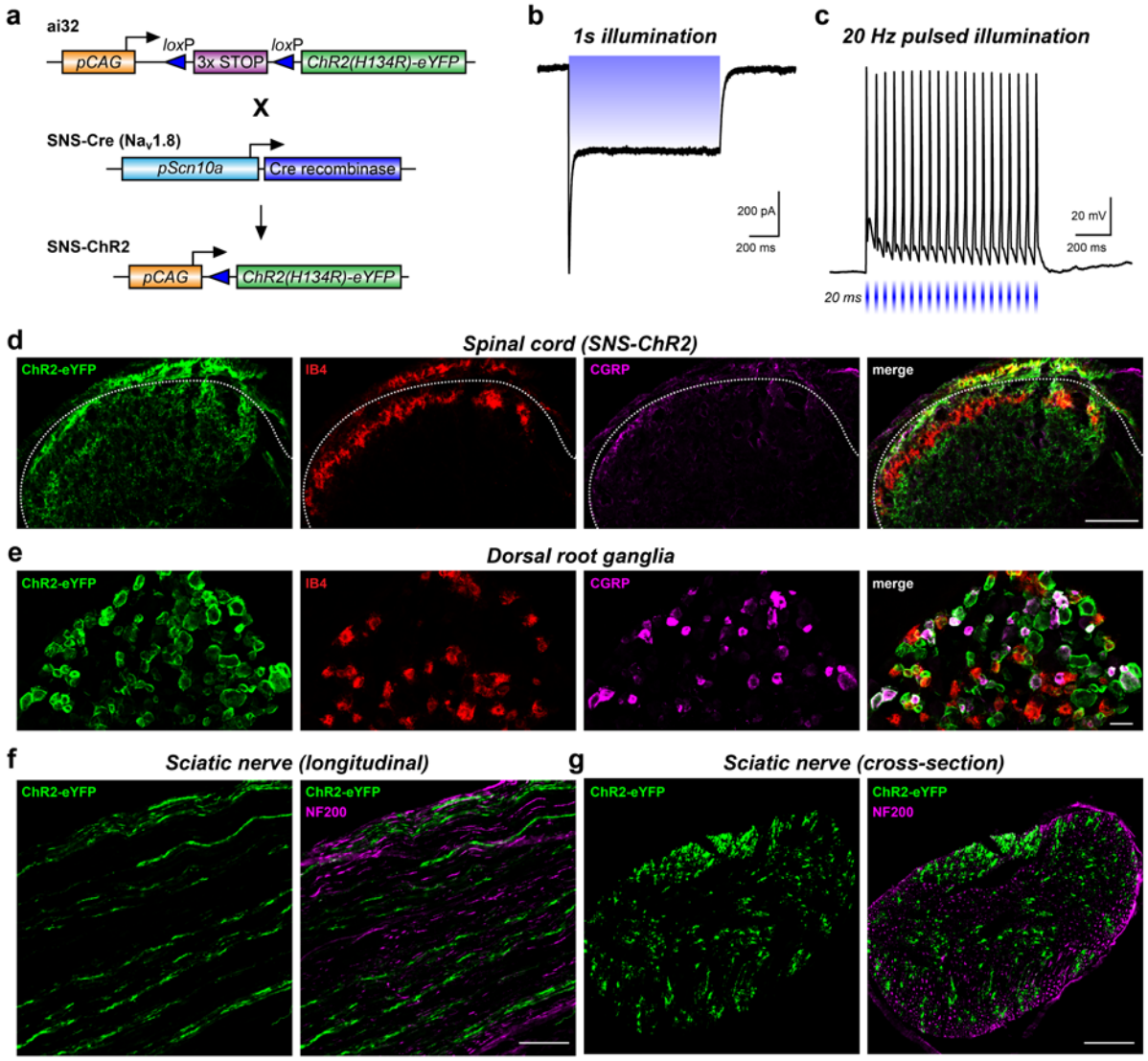

Supplementary Fig. 14

Electrophysiological and anatomical characterization of ChR2 expression in SNS-Ai32 mice. (a) Schematic of the Ai32 locus and SNS-Cre locus, together with results of the cre-dependent recombination of the Ai32 locus. (b) Inward current in cultured sensory neurons from the SNS-ChR2 mice. (c) In current clamp, 20 Hz pulsed illumination results in high-fidelity action potential firing in SNS-ChR2 mice. (d) Immunohistochemical analysis of tissue from adult SNS-Ai32 mice demonstrates that ChR2 is expressed along the peripheral neuraxis, including termination in lamina I and lamina II of the spinal cord dorsal horn as evidenced by overlap with CGRP (purple) and IB4 (red), respectively. (e) Staining of DRG demonstrates significant overlap

of expression with CGRP (purple) and IB4 (red) within the soma, and longitudinal (f) and cross sections (g) of sciatic nerve demonstrate robust staining along the plasma membrane of the axons. This expression pattern, as expected is more restricted than in Advillin-Ai32 mice. Scale bars = 100μm.

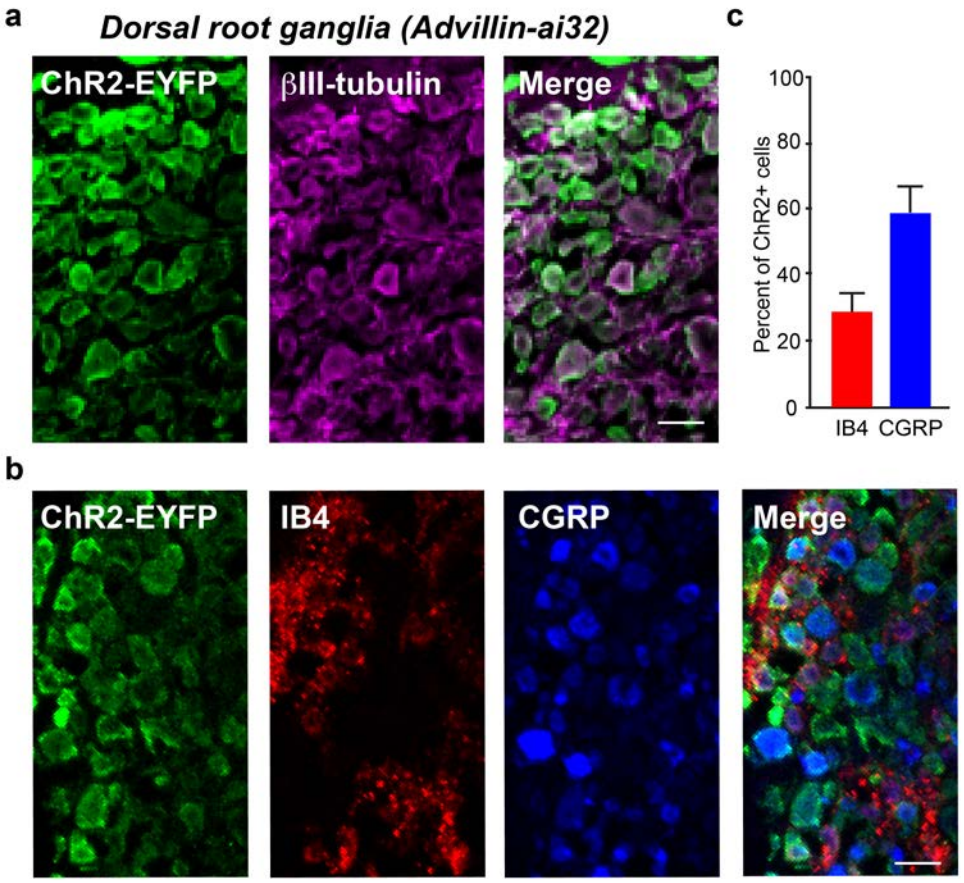

Supplementary Fig. 15

Immunohistochemical characterization of dorsal root ganglion ChR2 expression in Advillin-ChR2 mice. (a) Immunohistochemical analysis of DRG from adult Advillin-Ai32 mice demonstrates significant overlap (82 % ± 3 %) of ChR2-EYFP (green) expression with βIII tubulin (purple) within the soma. (b) Staining of DRG demonstrates the expression of ChR2-EYFP (green) within the subpopulation of non-peptidergic neurons, identified through labeling for IB4 (red), and subpopulation of peptidergic neurons, identified through labeling for CGRP (blue). (c) Quantification of the ChR2-EYFP expressing neurons shows that 29 ± 6 % of ChR2 positive neurons co-label with the non-peptidergic population and 57 ± 8 % co-label with the peptidergic (CGRP) population. Scale bars = 50 μm.

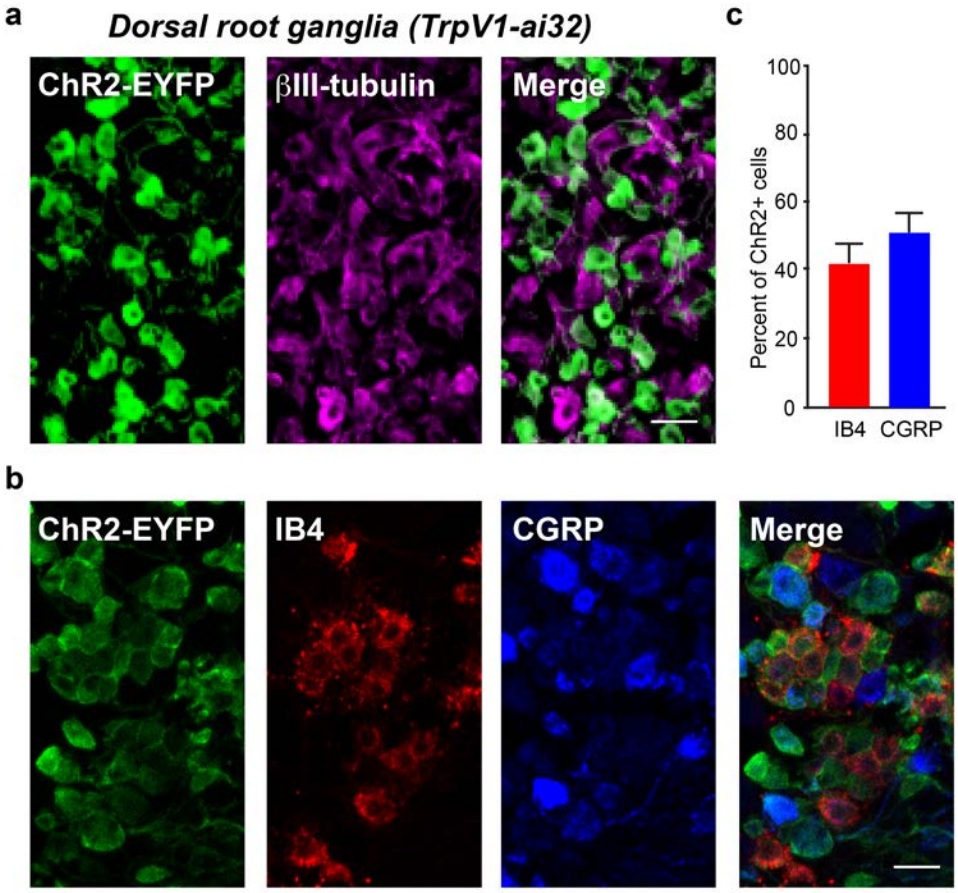

Supplementary Fig. 16

Immunohistochemical characterization of dorsal root ganglion ChR2 expression in TrpV1-ChR2 mice. (a) Immunohistochemical analysis of DRG from adult TrpV1-Ai32 mice demonstrates significant overlap (59 ± 3 %) of ChR2-EYFP (green) expression with βIII tubulin (purple) within the soma. (b) Staining of DRG demonstrates the expression of ChR2-EYFP (green) within the subpopulation of non-peptidergic neurons, identified through labeling for IB4 (red), and subpopulation of peptidergic neurons, identified through labeling for CGRP (blue). (c) Quantification of ChR2-EYFP expressing neurons shows that 41 ± 5 % of ChR2 positive neurons co-label with the non-peptidergic (IB4) population and 51 ± 7 % co-label with the peptidergic (CGRP) population. Scale bars = 50 μm.

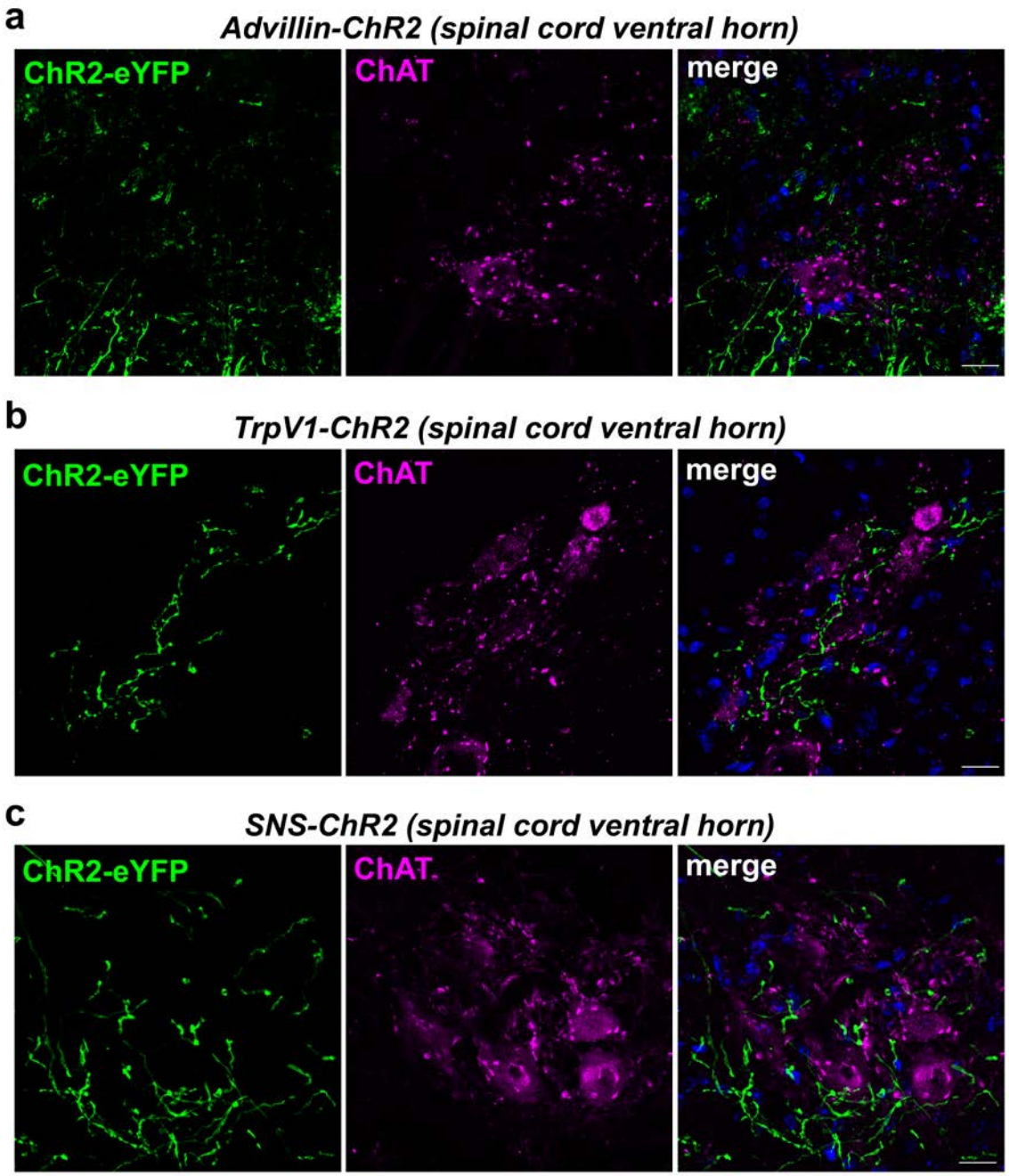

Supplementary Fig. 17

Characterization of ChR2-EYFP expression in the ventral horn of the spinal cord of Advillin-ChR2, TrpV1-ChR2, and SNS-ChR2 mice. Confocal images of the spinal cord ventral horn from Advillin-ChR2 (a), TrpV1-ChR2 (b) and SNS-ChR2 (c) mice, showing sparse $ChR2^{+}$ fibers (green) innervating deeper lamina. Motor neurons are marked by choline acetlytransferase

(ChAT, purple). We did not observe ChR2 expression in motor neurons of any of these transgenic lines. The scale bar indicates 20 μm for all panels.

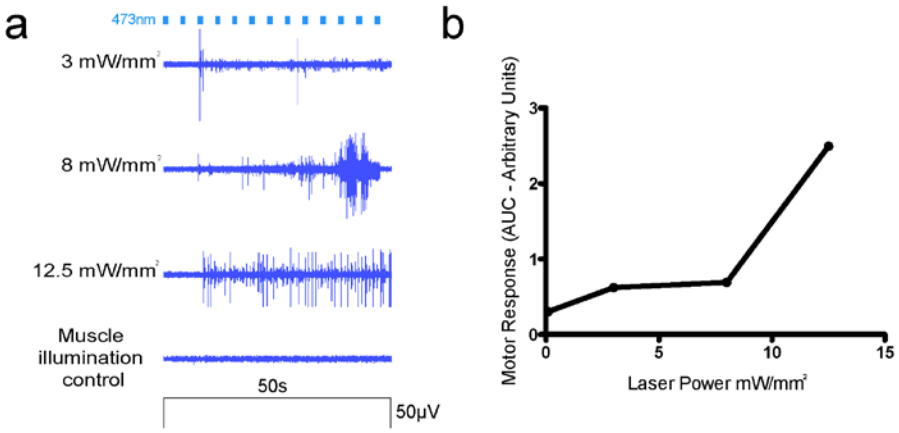

Supplementary Fig. 18

Direct laser activation of the sciatic nerve in an open preparation. Blue fiber-optic laser illumination of the exposed sciatic nerve in lightly anesthetized TrpV1-ChR2 mice produces reflexive withdrawal behaviors. (a) EMG tracing showing quadriceps contractions during blue-laser illumination of the exposed sciatic nerve ranging between 3 - 12.5 mW/mm^2. In the bottom trace, the laser illuminated the muscle on top of the sciatic nerve, but not the nerve itself and evoked no motor response. This is consistent with the muscle contractions being a reflexive response to optogenetic excitation of the axons by blue light. (b) Quantification of the EMG recordings from the quadriceps during laser illumination of the sciatic. Motor response (area under the curve – arbitrary units) increased as the laser power increased.

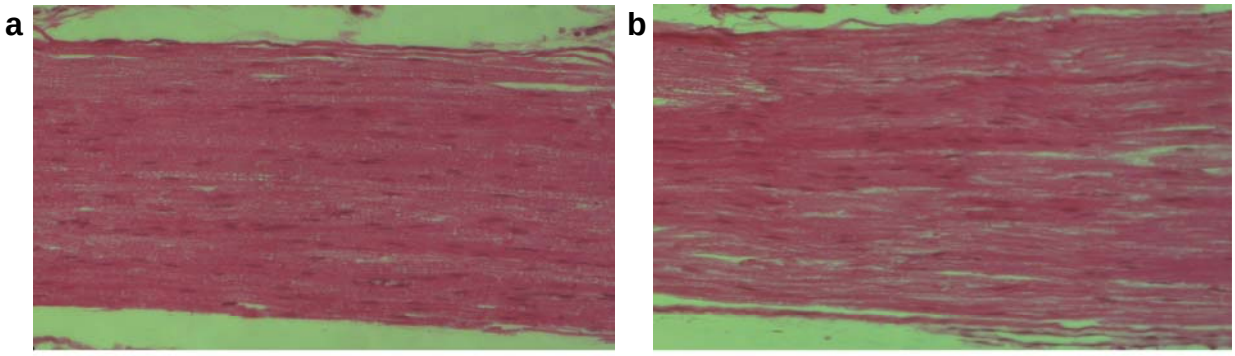

Supplementary Fig. 19

Hematoxylin and eosin (H&E) staining of sciatic nerves taken from C57BL/6J wild type mice at 16x magnification. (a) is a representative ipsilateral nerve which has been interfaced with the sciatic optogenetic simulator for 1 month. (b) is the contralateral nerve from the same animal utilized for comparison. No gross infiltration was noted using standard H&E techniques to observe neutrophils, lymphocytes, monocytes, basophils, eosinophils, red blood cells, or lipofuschin.

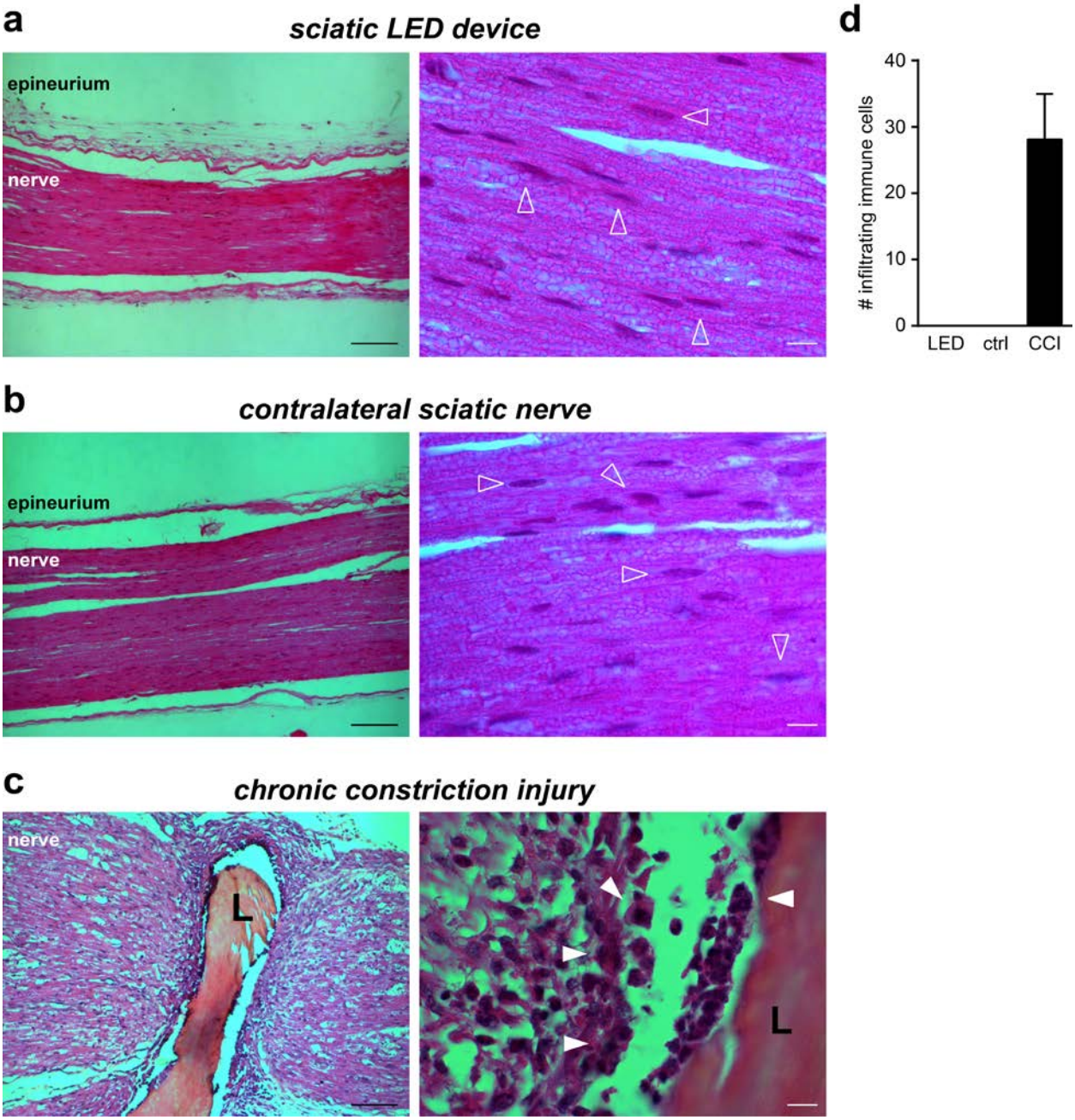

Supplementary Fig. 20.

Histological analysis of the sciatic nerve after peripheral nerve device implantation or the chronic constriction injury procedure. (a)-(c) Transmitted light micrographs of haematoxylin (purple) and eosin (pink) staining of longitudinal sciatic nerve sections taken at 10x (left) and 63x (right). Panels in (a) show sections of the sciatic nerve from a mouse with a peripheral device implanted for 2 weeks. The LEDs were positioned in the middle of this section of nerve.

Open arrowheads highlight the flattened nuclei of myelinating Schwann cells (purple). Images in (b) are from the contralateral nerve. Sciatic nerve sections in (c) are from a mouse that had a chronic constriction injury surgery (CCI), a model for neuropathic pain. Note the large number of infiltrating immune cells, identified by their multi-lobed nuclei (closed arrowheads) surrounding the ligature (L) and the prominent swelling of the nerve due to inflammation. (d) Quantification of immune cell infiltration in 63x images of the sciatic. No immune cells were identified in device-implanted animals (LED), the contralateral control sections (ctrl). However we observed 28 ± 7 immune cells per section from CCI mice. Quantification was performed on 2 - 4 sections from 3-4 mice for each condition; data represent mean ± sem. Scale bars are 100 μm for 10x images and 10 μm for 63x images.

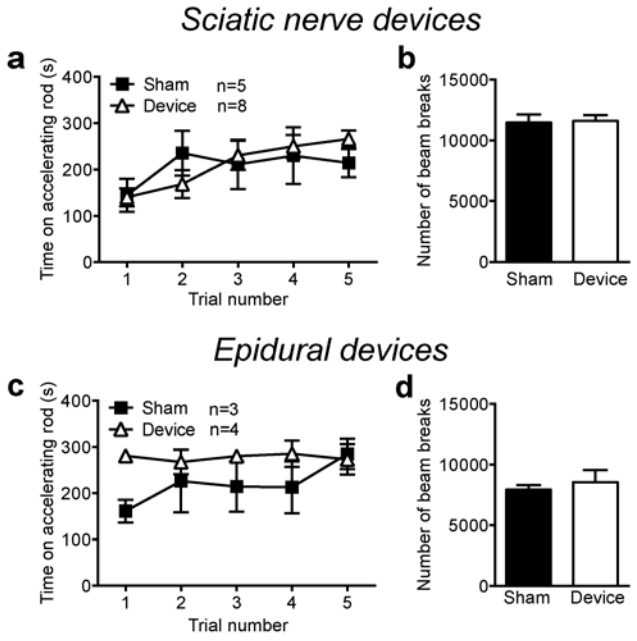

Supplementary Fig. 21

Characterization of locomotor activity after sciatic and epidural device implantation using the open field and accelerating rotarod tests. (a) Accelerating rotarod testing of C57BL/6J wild type mice implanted with sciatic nerve devices (n = 8) versus sham-operated littermates (n = 5) at one week post-implantation. Two-way ANOVA revealed no significant difference (p = 0.891) between the two groups. (b) Open field testing of locomotor activity of C57BL/6J wildtype mice implanted with optogenetic sciatic nerve stimulators (n = 8) versus sham-operated littermates (n = 5) at one week post-implantation. A T-test revealed no significant difference between the two groups (p = 0.886). (c) Accelerating rotarod testing of C57BL/6J wild type mice implanted with epidural devices (n = 4) versus sham-operated littermates (n = 3) at one week post-implantation. Two-way ANOVA revealed no significant difference (p = 0.226) between the two groups. (d) Open field testing of locomotor activity of C57BL/6J wild type mice implanted with epidural devices versus sham-operated littermates at one week post-implantation (n = 3 per group). A T-test revealed no significant difference between the two groups (p = 0.589).

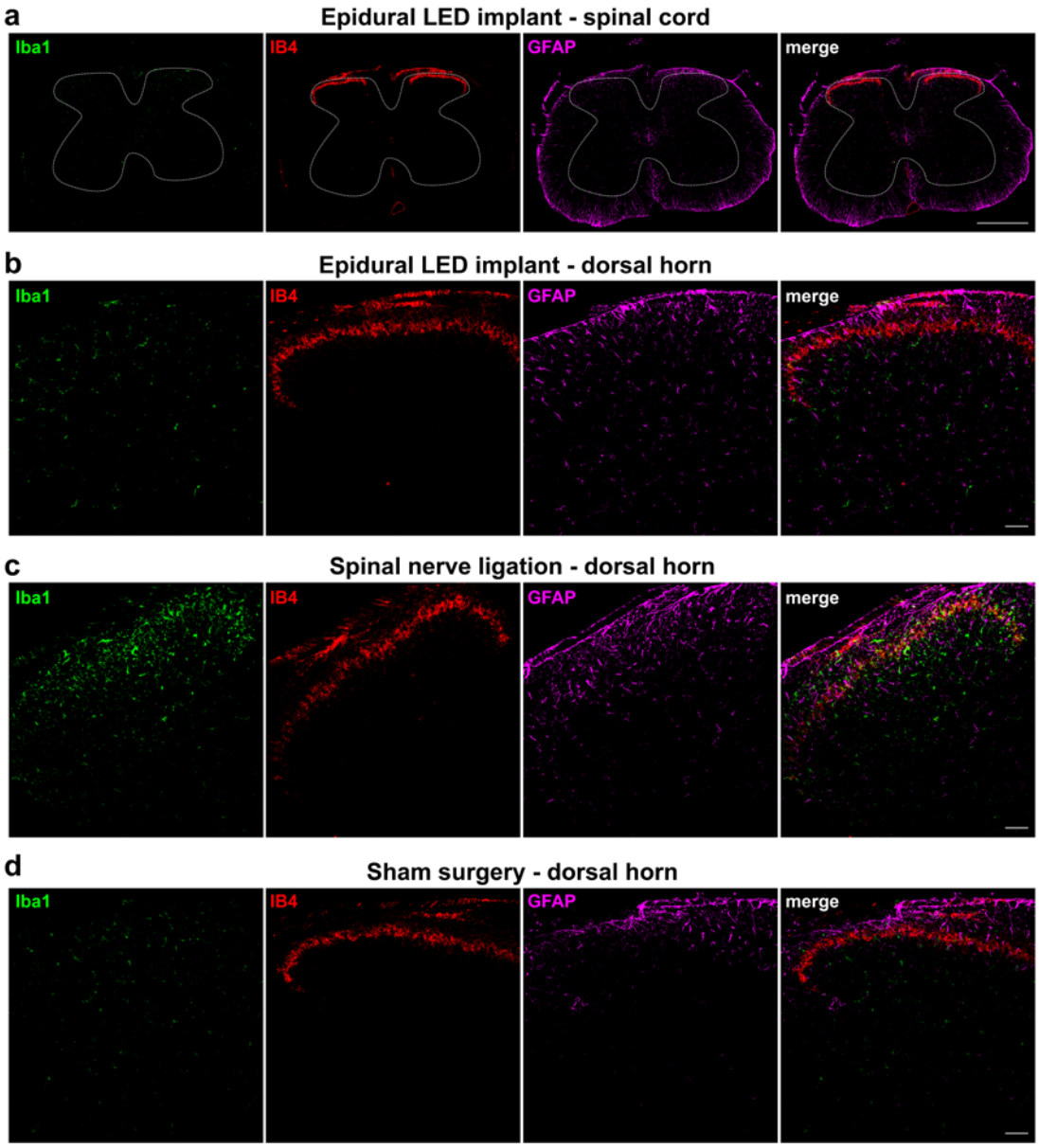

Supplementary Fig. 22

Immunohistological analysis of the dorsal horn of the spinal cord after either epidural device implantation or the spinal nerve ligation procedure. (a) Low power confocal micrograph of a transverse section of the lumbar spinal cord from a mouse with an epidural LED device implanted in the epidural space for two weeks. Iba1 (green) labels activated microglia, IB4 (red) labels non-peptidergic sensory afferents in lamina II of the dorsal horn, and GFAP (purple) marks astrocytes. The dotted line outlines the spinal cord gray matter. Scale bar is 500 μm. (b) Higher power confocal images of the dorsal horn of the lumbar spinal cord from a mouse with an

epidural LED device implanted for two weeks. Sections were labeled for markers of activated microglia (Iba1, green), non-peptidergic fibers in the dorsal horn (IB4, red), and astrocytes (GFAP, purple). We did not observe the presence of activated microglia or proliferating astrocytes in implanted mice. Scale bar is 50 μm. (c) Spinal cord dorsal horn sections five days after ligation of the L4 spinal nerve. Notice the prominent labeling of activated microglia (green) and astrocyte proliferation (purple). Scale bar is 50 μm. (d) Spinal cord dorsal horn sections from a mouse that underwent a laminectomy but was not implanted with an epidural LED device. We did not detect prominent activation of microglia or increased astrocyte proliferation following the simple laminectomy. Scale bar is 50 μm.

Process	Purpose	Required time for 10 devices	Equipment	Progress level (%)
1. Preparation of PMMA coated glass	Sampling for transfer	1 hour	Cleanroom Spin-coater	5
2. PI film fabrication	Bottom encapsulating layer	3 hours	Cleanroom, Vacuum oven	15
3. Metal (Ti/Au) deposition	Interconnection	3 hours	E-beam deposition	25
4. Metal patterning		2 hours	Cleanroom, Mask aligner	30
5. PI encapsulation	Top encapsulating layer	3 hours	Cleanroom, Vacuum oven	40
6. PI/Metal/PI patterning	Patterning for stretchable circuits	2 hours	Cleanroom, mask aligner,	50
7. PI etching		3 hours	RIE	60
6. Components transfer	Active components integration	5 hours	Solder, Microscope	80
7. PDMS encapsulation	System packaging	1 hour	Oven	100

Supplementary Table 1: Fabrication process details

Parameter	TrpV1-ChR2
Rise time	2.4 ± 0.2 ms
Peak amplitude	261.1 ± 53.1 pA
tau	12.5 ± 1.0 ms
Steady state	98.4 ± 20.0 pA
% Steady state	37.6 ± 0.5
APs fired in response to a 10 Hz stimulus lasting 2, 5, or 10 ms	6 ± 3
APs fired in response to a 20 Hz stimulus lasting 20 ms	7 ± 3

Supplementary Table 2: Electrophysiological properties of ChR2-expressing sensory neurons in response to optical stimuli, rise time, peak amplitude, tau, steady state and percent steady state. These parameters are based on a 470 nm, 10 mW/mm^2 light pulse that was 1s in length (n = 9). The number of action potentials fired to a 10 Hz stimulus is a result of pooling the responses to 470 nm, 10 mW/mm^2 light pulses lasting either 2, 5 or 10 ms in length (n = 4). The number of action potentials fired to a 20 Hz stimulus is a result of a 470 nm, 10 mW/mm^2 light pulse 20 ms in length (n = 6). AP; action potential. Data are presented as mean ± standard error of the mean.

Supplementary Movie 1: Device implantation does not inhibit exercise behavior

Clip of a mouse with a green sciatic nerve LED device running on an exercise wheel without any limitations.